JGR Atmospheres

RESEARCH ARTICLE
10.1029/2020JD033412

Kelvin-Helmholtz Billow Interactions and Instabilities in the Mesosphere Over the Andes Lidar Observatory: 2. Modeling and Interpretation

David C. Fritts[1,2], Scott A. Wieland[1,2], Thomas S. Lund[1], S. A. Thorpe[3], and James H. Hecht[4]

[1]GATS, Boulder, CO, USA, [2]Embry-Riddle Aeronautical University, Daytona Beach, FL, USA, [3]School of Ocean Sciences, Bangor University, Anglesey, UK, [4]The Aerospace Corporation, El Segundo, CA, USA

This article is a companion to Hecht et al. (2020), https://doi.org/10.1029/2020JD033414.

Key Points:
- Variations in the thickness of an unstable shear layer cause KH billows to have different scales and alignments at adjacent locations
- Interactions among misaligned KH billows cause "tubes" and "knots" that are distinct from secondary instabilities of individual billows
- Instability dynamics of interacting KH billows can be much more intense and energetic than those of individual billows

Supporting Information:
- Supporting Information S1

Correspondence to:
D. C. Fritts,
dave@gats-inc.com

Citation:
Fritts, D. C., Wieland, S. A., Lund, T. S., Thorpe, S. A., & Hecht, J. H. (2021). Kelvin-Helmholtz billow interactions and instabilities in the mesosphere over the Andes Lidar Observatory: 2. Modeling and interpretation. *Journal of Geophysical Research: Atmospheres*, *126*, e2020JD033412. https://doi.org/10.1029/2020JD033412

Received 1 JUL 2020
Accepted 25 SEP 2020
Accepted article online 9 NOV 2020

Author Contributions:
Conceptualization: David C. Fritts
Formal analysis: David C. Fritts
Funding acquisition: David C. Fritts, James H. Hecht
Investigation: David C. Fritts, Scott A. Wieland, Thomas S. Lund, S. A. Thorpe, James H. Hecht
(continued)

Abstract A companion paper by Hecht et al. (2020, https://doi.org/10.1002/2014JD021833) describes high-resolution observations in the hydroxyl (OH) airglow layer of interactions among adjacent Kelvin-Helmholtz instabilities (KHI). The interactions in this case were apparently induced by gravity waves propagating nearly orthogonally to the KHI orientations, became strong as Kelvin-Helmholtz (KH) billows achieved large amplitudes, and included features named "tubes" and "knots" in early laboratory KHI studies. A numerical modeling study approximating the KHI environment and revealing the dynamics of knots and tubes is described here. These features arise where KH billows are misaligned along their axes or where two billows must merge with one. They bear a close resemblance to the observed instability dynamics and suggest that they are likely to occur wherever KHI formation is modulated by variable wind shears, stability, or larger-scale motions. Small-scale features typical of those in turbulence develop in association with the formation of the knots and tubes earlier and more rapidly than those accompanying individual billows, supporting an earlier conjecture that tubes and knots are commonly major sources of intense turbulent dissipation accompanying KHI events in the atmosphere.

1. Introduction

Kelvin-Helmholtz instability (KHI; Helmholtz, 1868; Kelvin, 1871) is known to play major roles in sheared and stratified fluids. The first studies in the atmosphere and ocean were made at roughly the same times and showed that these dynamics share common features, despite a very different Prandtl number and often different scales. Early atmospheric studies employed noctilucent cloud (NLC) imaging at high altitudes (Witt, 1962) and multiple cloud observations and radar measurements in the troposphere (e.g., Gossard et al., 1973; Ludlam, 1967; Richter, 1969; Scorer, 1951, 1969). Initial ocean studies employed dyes that revealed Kelvin-Helmholtz (KH) billows and the structures of the surrounding environments (Woods, 1968, 1969; Woods & Wiley, 1972). KH billows were also observed in a deep lake using vertical arrays of thermistors (Thorpe, 1978; Thorpe et al., 1977).

These and subsequent studies revealed many details of KHI environmental dependence and transitions to turbulence. Browning and Watkins (1970) and Woods and Wiley (1972) described KH billow growth, transition to turbulence, and emergence of a mixed layer resulting in higher shear and stability at its edges in the atmosphere and ocean (Fritts & Rastogi, 1985; Thorpe, 2005). Early laboratory and modeling studies confirmed predictions of billow wavelength dependence on shear depths and revealed the dependence of KH billow amplitudes on Richardson number, Ri (Patnaik et al., 1976; Thorpe, 1971, 1973a, 1973b). Laboratory and modeling studies also revealed the character of secondary instabilities leading to turbulence for sufficiently high Reynolds number, Re.

Instabilities within KH billows comprise longitudinal counterrotating convective rolls at moderate and higher Re ~ 300–4,000 (Fritts, Baumgarten, et al., 2014; Fritts, Wan, et al., 2014; Klaassen & Peltier, 1985; Palmer et al., 1996; Schowalter et al., 1994; Thorpe, 1985, 1987; Werne & Fritts, 1999). Secondary KHI in the stable braids between adjacent billows, in contrast, were only observed in modeling and laboratory studies at higher Re (Corcos & Sherman, 1976; Fritts et al., 2012; Thorpe, 1987). Where they arise, the scales of these secondary instabilities, relative to the KHI horizontal wavelength, λ_h, decrease with increasing Re because reduced viscosity allows attainment of thinner sheared and convectively unstable layers in the

Methodology: David C. Fritts, Scott A. Wieland
Resources: David C. Fritts
Software: Thomas S. Lund, James H. Hecht
Supervision: David C. Fritts
Visualization: Scott A. Wieland
Writing - original draft: David C. Fritts
Writing – review & editing: David C. Fritts, S. A. Thorpe, James H. Hecht

outer KH billows and thinner vorticity sheets in the stable braids (Fritts, Baumgarten, et al., 2014; Klaassen & Peltier, 1985; Palmer et al., 1996; Werne & Fritts, 1999). Reviews of earlier studies were provided by Thorpe (1973a, 1985, 1987) and Fritts and Rastogi (1985).

KHI occurrence in the atmosphere and oceans is often induced by gravity waves (GWs) having lower and higher intrinsic frequencies and attaining enhanced local shears or large amplitudes (Dunkerton, 1997; Fritts & Alexander, 2003; Lelong & Dunkerton, 1998; Woods, 1968). At higher GW frequencies, these responses often manifest as descending KHI events following the most unstable shears occurring at the peak upward displacements within larger-scale GWs (Baumgarten & Fritts, 2014; Fritts et al., 2013; Fritts, Baumgarten, et al., 2014; Lehmacher et al., 2007; Pfrommer et al., 2009).

Of primary interest in this paper are KH instabilities that arise due to interactions of adjacent KH billows as they achieve finite amplitudes. These are a result of deformations of KH billow cores where the axes of adjacent KH billows are misaligned. Such deformations and misalignments were noted in early observations of thin cloud layers by Witt (1962), Scorer and Wexler (1963), and Ludlam (1967); also, see the multiple subsequent studies discussed by Thorpe (2002) and the OH airglow observations by Hecht et al. (2005, 2014). Collectively, Thorpe (2002) estimated that early imaging and radar studies implied a typical ratio of KH billow core lengths to wavelengths of ~3–8. Ludlam (1967) also noted the increasing irregularity of KH billows in time, and Thorpe (2002) recognized that small-scale GWs propagating roughly normal to KH billow axes would modulate the *Ri* of the shear layer accounting for KHI occurrence.

Subsequent KH billow interaction dynamics, termed "tubes" and "knots" by Thorpe (1985, 1987), arise where growing KH billows occur in adjacent regions that impose either misaligned billows or different KH billow wavelengths, λ_h; see Hecht et al. (2014) and the companion paper by Hecht et al. (2020, hereafter H20). Where these emerging structures occur in close proximity, vortex tubes are seen to evolve that link misaligned billows and lead to strong, entwined vortex dynamics, or knots, that drive rapid transitions to strong local turbulence thereafter. See the descriptions, laboratory shadowgraphs, and artist's conceptions of these dynamics by Thorpe (1985, 1987, 2002), Caulfield et al. (1996), and Holt (1998). The event observed in the mesosphere by a high-resolution OH airglow imager (H20) motivated our modeling of these dynamics presented here.

H20 identified a dramatic KHI event in high-resolution OH airglow imaging from the Andes Lidar Observatory (ALO) at Cerro Pachon, Chile (30.3°S, 70.7°W, 2,530 m elevation) on 1 March 2016. The 50 × 50-km imager field of view (FOV) captured interactions among KH billows having λ_h ~ 7–10 km that arose due to modulation by a λ_h ~ 25–30-km GW propagating toward the NW roughly normal to the wind shear in the approximately NE-SW plane enabling KHI growth. GW modulation apparently yielded varying shear depths at the time of KHI initiation (as suggested by Thorpe, 2002) that led to bands of emerging KH billows aligned along the wind shear, but having differing λ_h and misaligned KH billows between adjacent bands along the KH billow axes.

The ALO OH imager provided 30-m spatial resolution, but 4 × 4 pixel binning to reduce image size, and employed image differencing with a Δt ~ 22 s. The difference imaging enabled high sensitivity to KHI and secondary instability dynamics that caused the majority of brightness variations on small temporal and spatial scales by removing brightness contributions by larger-scale and slowly varying features at other altitudes. These capabilities enabled characterization of the KHI event evolution, including emergence of KHI in narrow bands, growth and linking of misaligned KH billows across the initial gaps between bands, evidence for tube and knot dynamics accompanying these misaligned KH billows, and secondary convective instabilities (SCI) within individual billow cores, all of which subsequently contributed to driving turbulence transitions.

Our goals in this paper are to reveal and quantify the dynamics arising due to misaligned KH billows, specifically the tube and knot evolutions comprising these dynamics, their significance relative to secondary instabilities of individual KH billows, and the potential atmospheric impacts. To do so, we employ the Complex Geometry Compressible Atmosphere Model (CGCAM) in a local, Cartesian domain to simulate KH billow interactions in a region where billows in adjacent bands are misaligned due to different KHI wavelengths at either side.

Our paper is organized as follows. Section 2 provides a brief summary of the ALO observations motivating this modeling study. The CGCAM formulation, solution method, and initial and boundary conditions are described in section 3. CGCAM results are described and compared with the ALO observations in section 4. Section 5 discusses the relation of these dynamics to previous laboratory and atmospheric studies and implications for their importance in the atmosphere and other sheared and stratified fluids. Our summary and conclusions are provided in section 6.

2. Summary of KHI Interactions Over ALO

H20 described the first observations of KHI tube and knot dynamics occurring in a geophysical fluid at an altitude enabling large-scale KH billows and high-resolution imaging. The H20 interpretation of these observations was guided by laboratory studies discussed by Thorpe (1985, 1987) and enabled identification of specific features of KHI tube and knot dynamics. A summary of the dynamics revealed in high-resolution imaging and discussed by H20 is shown in Figure 1.

The six images in Figure 1 are differences between images separated by ~22 s at ~90-s intervals enabling high sensitivity to smaller-scale dynamics arising from KH billow deformations and misalignments driven by GW modulation of the underlying shear flow. The brighter features in Figure 1 aligned from lower left to upper right are the KH billows having initial λ_h ~ 7–10 km. The broader features having smaller brightness gradients aligned from upper left to lower right are GWs having λ_h ~ 25–30 km that modulated the underlying shear flow and stability and accounted for the misaligned KH billows seen along the darker phases between the regions showing stronger KHI.

The billows are bright for the chosen differencing because their roll-up imposes horizontal and vertical convergence and divergence in an environment having a mean vertical brightness gradient. They have bright edges because the largest brightness variations along the direction of feature advection (toward approximately NE along the shear flow) accompany the largest horizontal airglow brightness gradients, and these occur at the billow edges.

As described by H20, these images suggest a number of features revealed in earlier laboratory studies of KH billow evolutions and interactions by Thorpe (1985, 1987, and references therein). Inferences and specific features of these dynamics guided by the laboratory studies, theory, and earlier two- and three-dimensional (2-D and 3-D) modeling include the following:

1. a strong wind shear aligned approximately in the SW-NE (lower right to upper left) plane had a shear depth $2h \sim \lambda_h/2\pi$ ~ 1,200–1,600 m (Drazin, 1958; Holmboe, 1962),
2. *Ri* must have been small, ~0.1 or less, and *Re* was likely ~2,000 or larger, based on λ_h, inferred h, known kinematic viscosity (see below), and secondary CI scales,
3. modulation of the shear layer by a λ_h ~ 25-km GW propagating from roughly SE to NW and initiation of KH billows in a modulated initial shear led to KH billow deformations and misalignments along their axes (see white ovals in Figure 1 panel at 31:47),
4. KHI growth to finite amplitudes drove increasing interactions among adjacent KH billows along and normal to their axes (see Figure 1 panels from 33:19 to 36:19),
5. Intensifying shears between misaligned or distorted billows drove initial tube formation in the strong shears where one KH billow interacts with two (see yellow lines at 33:19 and thereafter),
6. roughly orthogonal tubes where KH billows are misaligned begin to interact, are advected over, under, and around each other where their "ends" become entwined by the single interacting KH billow, and lead to the initial stages of a vortex knot (see the panel at 34:47),
7. SCIs begin to emerge by 34:47 and intensify quickly thereafter (see the blue lines at 36:19),
8. The small-scale vortex dynamics intensify dramatically by 37:50, especially in the region of the initial vortex knot, and
9. The initial large-scale KH billows in this region largely disappear by 39:18, while others not affected as strongly by deformed or misaligned billow cores have not yet exhibited significant tubes, knots, or secondary instabilities.

Additional discussion of these dynamics and comparisons of the observed features with those seen in our modeling studies is provided in sections 4 and 5.

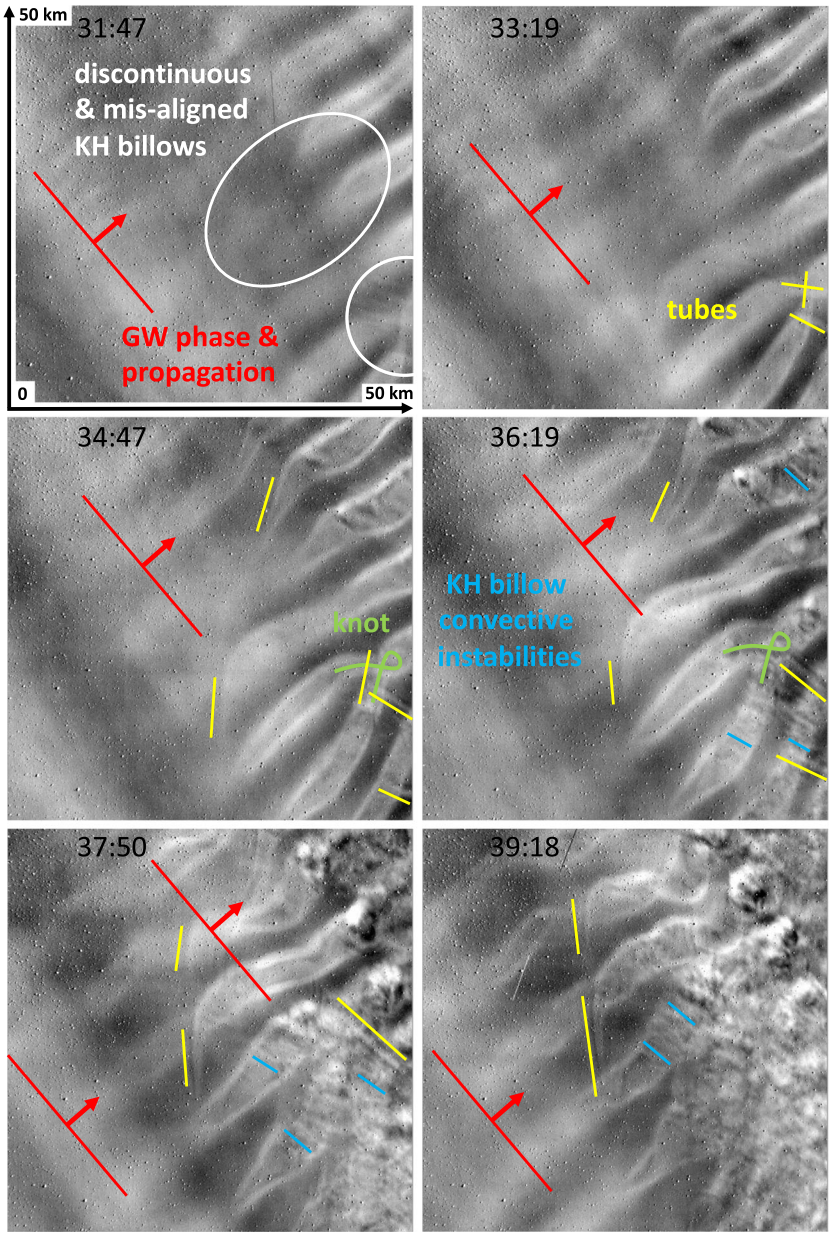

Figure 1. Differenced brightness images from H20 at ~90-s intervals showing emerging vorticity dynamics as KH billows that are deformed and/or misaligned evolve to larger amplitudes and exhibit various instability dynamics in an ~50 × 50-km field of view (with north at top and east at left). See the image dimensions at upper left and notation and highlights of the relevant features where they first arise and evolve thereafter.

3. CGCAM Description and Configuration

3.1. Governing Equations and Solution Method

CGCAM employs the finite-volume method described by Felten and Lund (2006) to discretize the compressible Navier-Stokes equations such that they result in exact numerical conservation of mass, momentum, and kinetic and thermal energy and thus faithfully represent the underlying conservation laws, apart from specified dissipation. These equations are expressed in strong conservation law (divergence) form written as

$$\frac{\partial \rho}{\partial t} + \frac{\partial \rho u_j}{\partial x_j} = 0 \tag{1}$$

$$\frac{\partial \rho u_i}{\partial t} + \frac{\partial \rho u_i u_j}{\partial x_j} = -\frac{\partial \rho}{\partial x_i} - \rho g \delta_{i3} + \frac{\partial \sigma_{ij}}{\partial x_j} \tag{2}$$

$$\frac{\partial \rho E}{\partial t} + \frac{\partial (\rho E + p) u_j}{\partial x_j} = -\rho g u_3 + \frac{\partial u_i \sigma_{ij}}{\partial x_j} - \frac{\partial q_j}{\partial x_j} \tag{3}$$

where σ_{ij} and q_j are the viscous stress and thermal conduction, defined as

$$\sigma_{ij} = \mu \left[\left(\frac{\partial u_i}{\partial x_i} + \frac{\partial u_j}{\partial x_i} \right) - \frac{2}{3} \left(\frac{\partial u_k}{\partial x_k} \right) \delta_{ij} \right] \tag{4}$$

$$q_j = -\kappa \frac{\partial T}{\partial x_j} \tag{5}$$

Here μ is the dynamic viscosity, κ is the thermal conductivity, δ_{ij} is the Kronecker delta, μ and κ depend on the temperature through Sutherland's law (White, 1974), $\nu = \mu/\rho$ is the kinematic viscosity, and the Prandtl number, $Pr = \nu/\kappa$, is assumed to be unity so as to require uniform resolution of smaller scales in the velocity and temperature fields.

The solution variables are the density ρ, momentum per unit volume ρu_i or (ρu, ρv, ρw), and total energy per unit volume is $E = e + u_k u_k/2 = c_v T + u_k u_k/2$, with velocity components (u_i, u_j, u_k) along (x, y, z) and repeated subscripts denote a sum over all Fourier components. Additionally, $c_v = R/(\gamma - 1)$ is the specific heat at constant volume, T is temperature, and pressure p appears as an auxiliary variable and is related to ρ and T through the ideal gas law, $p = \rho RT$.

CGCAM uses an explicit third-order Runge-Kutta scheme for time advancement and sponge layers at the upper and lower domain boundaries to remove any perturbations arising from the interior KHI dynamics. Additional model details are provided by Dong et al. (2020).

3.2. Configurations, Initial and Boundary Conditions, and Resolution

We employ CGCAM here for two different types of simulations:

1. four simulations to explore the misalignments of KH billows arising in a uniform shear layer with KHI initiated by random three-dimensional (3-D), small-amplitude initial noise fields in velocity, such as must always occur in the atmosphere, and
2. one simulation imposing different shear depths along the KH billows (spanwise direction) so as to specify different KH billow λ_h in different regions imposing a misalignment requiring one KH billow to link to two KH billows in the spanwise domain center.

The specifications of these two applications are described below.

3.2.1. KHI Due to Random Noise in a Uniform Shear Layer

Four CGCAM simulations (Cases 1–4) are performed to explore influences of random initial noise on emerging KH billow λ_h and alignments. These noise seeds yielded 3 initial λ_h in Cases 1 and 2 and 3 and 4 initial λ_h in Cases 3 and 4. These employed a computational domain of dimensions (X, Y, Z) = (27, 54, 15) km that was periodic in x and y and free slip with 900-m sponge layers at the upper and lower boundaries. A multiply-periodic x domain and a longer y domain were specified to allow varying KHI phases, λ_h, and coherence along y with minimal constraints by the periodic y domain. The x domain and initial shear depth were chosen specifically to enable 3 and 4 initial KHI λ_h along x, rather than 2 and 3 λ_h along x, because initial test simulations revealed a tendency for significant KH billow pairing (judged to be artificial) when only 2 or 3 KH λ_h where allowed.

The initial mean wind was specified as

$$U(z) = U_0 \, tanh[(z - z_0)/h] \tag{6}$$

with z_0 at the center of the vertical domain. Assuming an initial $Ri = N^2/(dU/dz)^2 = 0.05$, a constant temperature T, a representative buoyancy frequency $N = 0.02$ s^{-1}, and a shear layer half depth $h = 700$ m for

an expected KHI $\lambda_h \sim 4\pi h \sim 9$ km, the implied horizontal velocity was $U_0 \sim 62.6$ m/s. We also assumed $Re = U_0 h/\nu = 5{,}000$ to constrain the required resolution, but retain the potential to describe KH billow interactions and dynamics exhibiting vigorous instabilities leading to turbulence. This implies an effective turbulent kinematic viscosity, $\nu_{turb} = U_0 h/5{,}000 \sim 9$ m^2/s, somewhat larger than ν at these altitudes, and consistent with inferences of elevated ν_{turb} at these altitudes in previous studies (Fritts, Baumgarten, et al., 2014; Fritts, Wan, et al., 2014; Hecht et al., 2014, 2018) in cases where turbulence contributions are relatively weak. An isotropic resolution of ~50 m was used at the central altitudes, with exponential mesh stretching near the upper and lower boundaries to reduce computational demands. Finally, a random noise seed having $u_{rms} = 10^{-3}\ U_0$ was employed.

3.2.2. KHI in a Nonuniform Shear Layer

The CGCAM configuration specifying different shear depths and wind magnitudes (Case 5) was achieved (such that a uniform Ri along y is obtained) using a larger domain having dimensions of $(X, Y, Z) = (40, 80, 20)$ km that was periodic in x and employed free slip boundaries in y and z and 1-km sponge layers at the upper and lower boundaries. Asymptotic shear layer half depths of $h = 700$ and 933 m and maximum $U_0 = 62.6$ and 93.5 m/s were achieved with U_0 and h given by

$$U_0(y) = U_T\{1 - 0.125[1 - \tanh(y/y_0)]\} \tag{7}$$

and

$$h(y) = h_T\{1 - 0.125[1 - \tanh(y/y_0)]\} \tag{8}$$

where $U_T = 93.5$ m/s, $h_T = 933$ m, $y_0 = 5$ km, and $y = 0$ is the spanwise domain center. As for the cases with a uniform shear flow, $Ri = 0.05$, $Re = U_0 h/\nu = 5{,}000$ at $y = 0$ with larger and smaller Re by ~25% at larger and smaller y, and a noise seed having $u_{rms} = 10^{-3}\ U_0$ is employed. CGCAM also employs a dynamic Smagorinsky subgrid-scale scheme (Germano et al., 1991; Moin et al., 1991) that operates to mimic the energy drain due to unresolved turbulent motions, but it is not required here.

To aid interpretation of the vorticity dynamics accompanying KH billow interactions and tube and knot dynamics, we employ the (negative) eigenvalue (λ_2) of the tensor defined as $\boldsymbol{L} = \boldsymbol{\Omega}^2 + \boldsymbol{S}^2$, where $\boldsymbol{\Omega}$ and $\boldsymbol{S}$ are the rotation and strain tensors, with antisymmetric and symmetric components $\Omega_{ij} = (\partial u_j/\partial x_i) - (\partial u_i/\partial x_j)/2$ and $S_{ij} = (\partial u_j/\partial x_i) + (\partial u_i/\partial x_j)/2$, to identify flow features having strong rotational character (Jeong & Hussain, 1995). Large (negative) λ_2 correspond to flow features having the greatest rotational, as opposed to shearing, character (independent of orientation), and its magnitude is a measure of rotational intensity. Pure shearing motions, in contrast, make no contribution to λ_2. Thus, λ_2 represents sensitivity to a subset of total vorticity that comprises the majority of the turbulence field and allows us to follow the transition from initial instability structures, through vortex interactions and instabilities, to fully developed turbulence. See Andreassen et al. (1998) and Fritts et al. (1998, 2009) for example applications of λ_2 in defining vortex dynamics accompanying breaking GWs.

4. CGCAM Modeling of KH Billow Interactions

4.1. Influences of KHI Phase and λ_h Variability in Uniform Shear

Figure 2 shows KH billow alignments and interactions for Cases 1–4 arising from different noise seeds with x-y cross sections of T'/T at an interval of 0.5 buoyancy period ($T_b = 2\pi/N = 314$ s). In each case, the initial noise field defines the KH billow λ_h in the streamwise direction (x, left-to-right), their variable phases in the spanwise direction (y, top-to-bottom), and secondary instability character, phases, and scales as the billows attain finite amplitudes.

Case 1 and 2 evolutions in Figure 2 show the emergence of three KH billows having varying phase along y with 1 and 2 y locations, respectively, at which phase variations are initially discontinuous. Panels 1b and 2b reveal the rapid emergence at these sites of billow cores penetrating the $z = 0$ plane suggesting billow dynamics connecting misaligned billow cores extending above and/or below the initial shear layer. Panels 1c and 2c show that these sites exhibit more rapid instability development and transitions to smaller scales than seen elsewhere. Additional, weaker instability transitions are nevertheless seen where the initial

billows exhibit spanwise variability in phase or amplitude where initial billow cores are continuous (see the lower portions of panels 1c and 2c). These features are seen below to be initial secondary KHI arising on the stratified vortex sheets between adjacent billows where the underlying billow cores exhibit variable phase in y. Instabilities become much more intense in panels 1d and 2d, but these transitions are much less rapid where initial billow cores were more uniform spanwise at the initial times.

Cases 3 and 4 (lower two rows in Figure 2) differ from Cases 1 and 2 in that each also exhibits a limited region along y where the noise seeds lead to 4 rather than 3 billows across the x domain (see the lower portion of Case 3 and the lower-middle portion of Case 4). These necessarily induce misalignments among initial KH billow cores along y that exhibit similar dynamics to those discussed in Cases 1 and 2. In all cases, billow cores that appear discontinuous at the central shear layer will be seen below to connect to adjacent billow cores via increasingly intense vorticity dynamics that exhibit increasing complexity and rapid transitions to strong turbulence. These dynamics comprise the tubes and knots initially identified in the laboratory studies discussed above and are examined in greater detail below.

4.2. KH Billow Tube and Knot Dynamics Due to Misaligned KH Billows

We employ CGCAM to explore the dynamics of a KH tube and knot evolution for Case 5 with $Ri = 0.05$ and $Re = 5{,}000$, given their anticipated deep dynamics for KH $\lambda_h \sim 10$ and 13.3 km and $H \sim 4$ km. The initial shear flow leads to three and four KH billows at the left and right sides of the spanwise domain (positive and negative y, respectively). T'/T and vorticity magnitude $|\zeta|$ x-y cross sections at $z = 0$ are shown at 0.33 T_b intervals from the emergence of tubes and knots to knot breakdown to strong turbulence in Figures 3 and 4. The nondimensional kinetic energy spectrum along x averaged along y and over altitudes spanning the largest $|\zeta|$, and a comparison of the peak enstrophy $\Omega = |\zeta|^2$ with time for the knot region and for KH billows not undergoing mutual interactions, are shown in Figure 5. Three-dimensional volumes showing λ_2 evolutions of tubes and knots from above, and from above, positive y, and negative x (upstream with respect to flow below the shear layer) spanning 1 and 2 T_b, respectively, are shown in Figures 6 and 7 (also see supporting information Movies S1–S3). The vorticity of the initial shear, $\zeta_y = \partial u/\partial z$, is toward the left ($y > 0$) in Figures 3, 4, and 6 and toward the lower left in Figure 7. Figure 8 shows depictions of vortex tube interactions and responses to initial perturbations leading to twist wave generation to aid our discussion. Figure 9 provides rotated views of the 3-D λ_2 evolution from the side, below, and above, and Figure 10 shows comparisons of the simulated tube and knot features with those seen in the laboratory by Thorpe (1987).

x-y cross sections of T'/T shown in Figure 3 reveal a simpler KH alignment than arise in Cases 1–4 because of the prescribed change in shear depth at central y. This narrow region in y has a single, discontinuous billow core at right apparently beginning to link with two billow cores at left (Figure 3a), which leads to strong interactions and rapid transitions to smaller-scale motions at these sites (Figure 3b). Because adjacent billows along x at smaller and larger y are also distorted, however, especially the nearest adjacent billow cores at right, the initial vortex interactions expand along the transition between three and four KH billows and lead rapidly to expanded strong interactions along x and a breakdown and disappearance of the initial coherent billow cores in this region within ~1 T_b.

Figure 4 showing $|\zeta|$ provides additional evidence of these interactions, instabilities, and the generation of smaller turbulence scales but also confined to the x-y plane at the initial shear layer. These fields reveal more clearly the initial confinement of these dynamics (Figure 4a), the rapid intensification and transition to turbulence (Figure 4b), and the expansion of these dynamics and disappearance of the billow cores extending along x within ~1 T_b (Figures 4c and 4d).

The 2-D fields at $z = 0$ cannot provide an understanding of the increasingly complex dynamics that account for this evolution. To do this, we employ 3-D volumetric views of the evolving vorticity dynamics revealed by λ_2, as employed in previous studies of transitions to turbulence accompanying GW breaking in sheared and unsheared flows (see Andreassen et al., 1998; Fritts et al., 1998, 2009).

To validate these fields and their descriptions of the KH billow interactions leading to tubes and knots, Figure 5a shows the CGCAM kinetic energy spectrum, $E(k)$, along x averaged in y and z at the final time shown in Figures 3 and 4. This is consistent with expectations of a –(5/3) spectral slope within the turbulence inertial range (dashed line), suggesting well resolved dynamics into the inertial range and without an artificial energy accumulation near the Nyquist wavenumber due to under-resolved small scales. Figure 5b shows

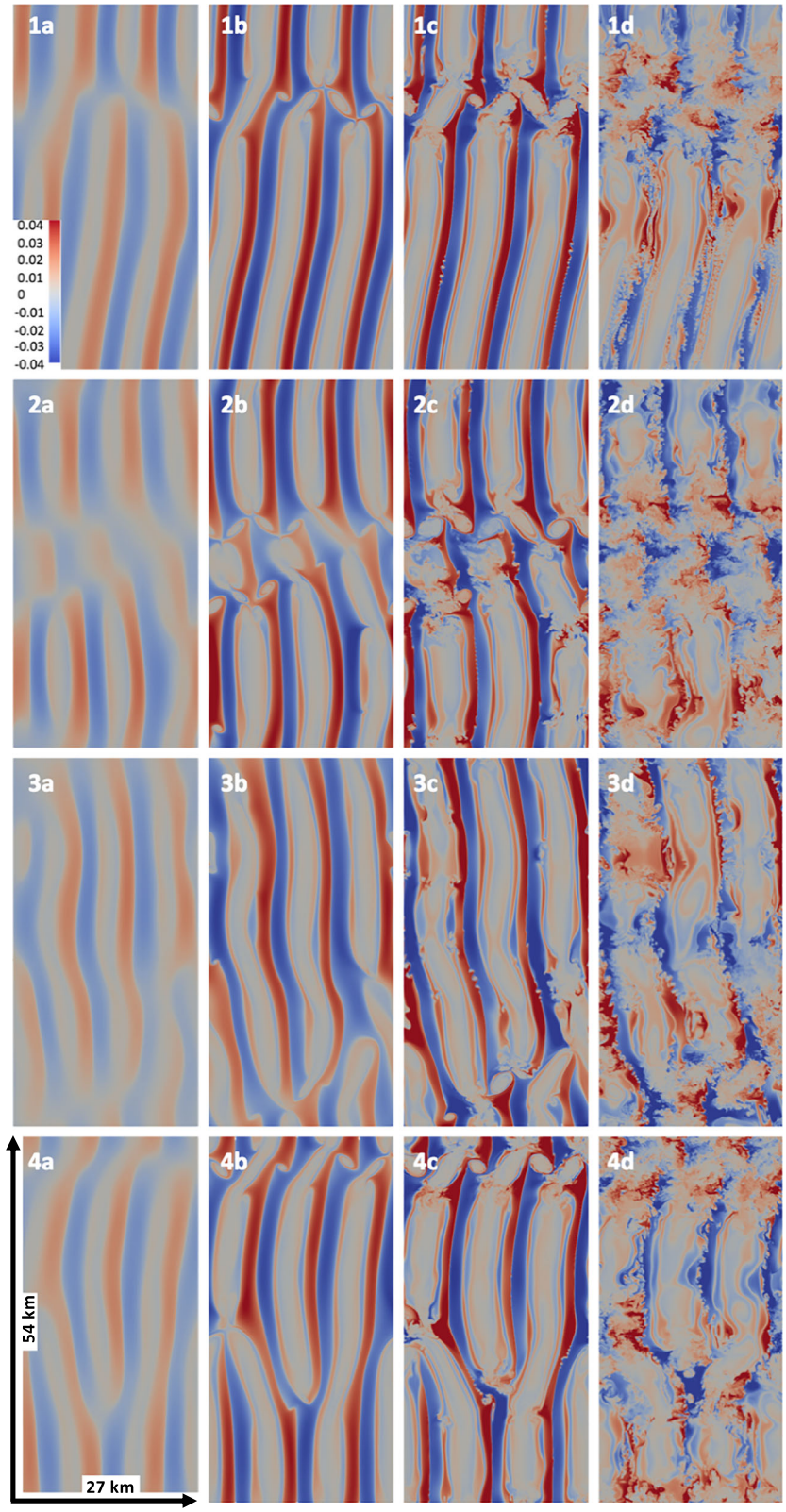

Figure 2. (top to bottom) Four CGCAM KH billow evolutions in $T'/T(x, y)$ at $z = 0$ (Cases 1–4), viewed from above spanning 1.5 *Tb* and arising from different initial noise fields in a domain allowing three or four KH billows along x (toward right). KH billow motions above $z = 0$ are toward right, and $T'/T < 0$ (>0) at left (right) are largest in the outer portions of the billows (see color scale in panel 1a). Axes and domain scales are shown in panel 4a.

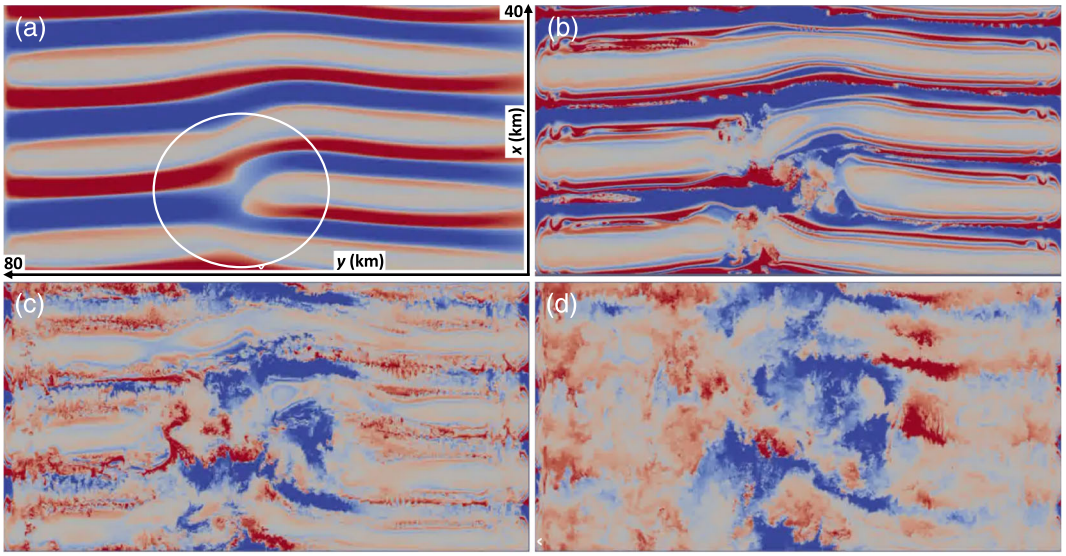

Figure 3. (a–d) Case 5 $T'/T(x, y)$ at $z = 0$ viewed from above (see axes in panel a). The upper flow at $z > 0$ is toward the top, positive mean ζ_y is toward positive y, and the color scale is as in Figure 1. Images span ~3 T_b, and the white oval in panel (a) shows the region in which billow interactions leading to vortex tubes first arise.

the dynamics of tubes and knots to also achieve large mean enstrophy, <Ω>, substantially larger than, and more than ~0.5 T_b before, that arising due to individual KH billows.

Three-dimensional images displayed in Figure 6 at early times reveal initial connections between adjacent, but misaligned, billow cores. This 3-D λ_2 evolution reveals the emergence of vortex tubes that arise in the

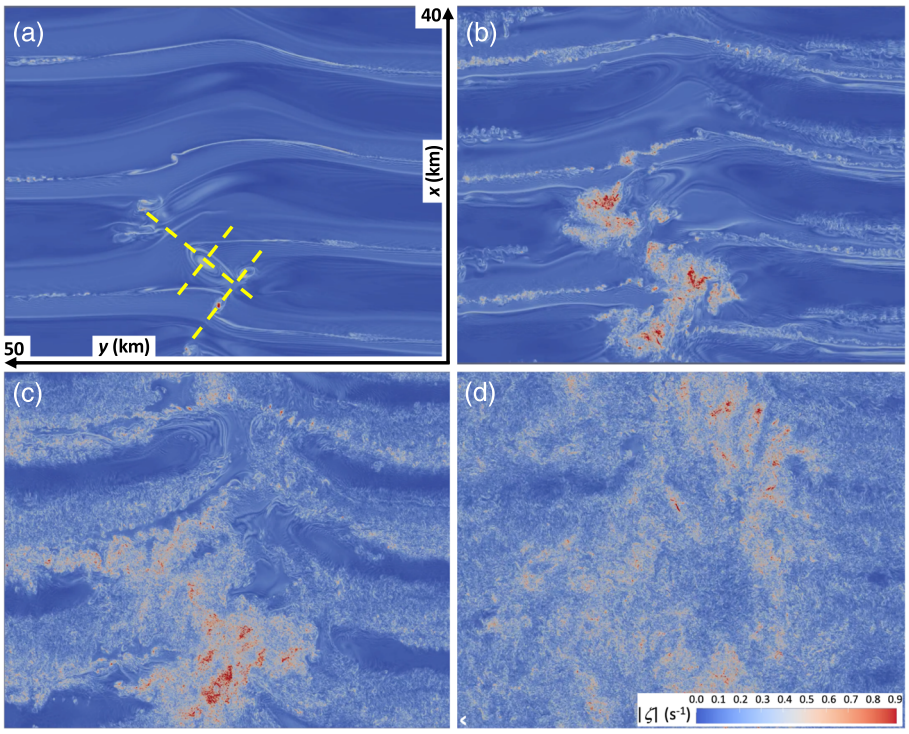

Figure 4. As in Figure 3, but showing $|\zeta|(x, y)$. The color scale is shown in panel (d). Dashed yellow lines in panel a show sites of initial vortex tube formation for comparison with Figures 6 and 7.

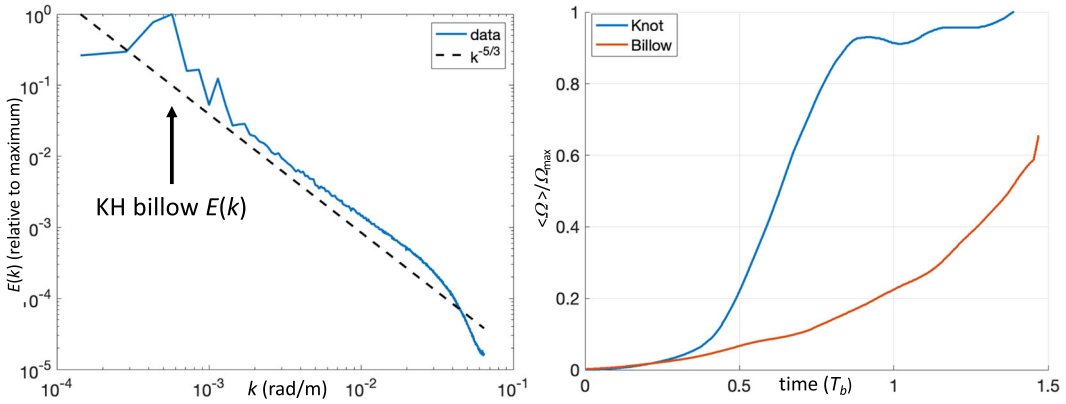

Figure 5. (left) Kinetic energy spectrum along x, $E(k)$, averaged in y and z at the final time shown in Figures 3 and 4; (right) mean enstrophy for KH billows leading to tubes and knots (blue) and for individual KH billows having only secondary KHI and CI for the same mean fields (red). Peak KH billow $E(k)$ is at $k = 2\pi/\lambda_x$ for λ_x ~ 10–13 km, thus ~100 times the Nyquist at ~100 m. Time at right is relative to the initial images in Figures 3 and 4.

intermediate vortex sheets extending along y between discontinuous billows along y rather than between side-by-side billow cores along x. Differential advection of the initial vortex sheet by emerging KH billows contributes to stretching and deformation that rotates and intensifies the vortex sheets and leads to their roughly orthogonal alignments and rollup into vortex tubes (see the emerging light green features in Figure 6a).

Rotation and stretching arises due to upward and forward advection (toward the top and out of the image plane at Site A in Figure 6a) by KH Billow 1 forward and right of the emerging tube and downward and rearward advection (toward the bottom and into the image plane at Site B) by KH Billow 2. These advective tendencies and vortex stretching lead to increasing positive ζ_y and increasing negative streamwise vorticity, $\zeta_x < 0$ (downward, toward negative x), between A and B.

The same advective tendencies at Sites C and D as at A and B, but with opposite consequences, account for the opposite alignment attained by the tube extending from C to D (increasing ζ_y and increasing positive streamwise vorticity, $\zeta_x > 0$, between C and D). The vortex sheet and emerging vortex tube extending from E to F replicates the dynamics of that from A to B. At each site where two tubes have emerged at a single billow core (Billows 2 and 3), the rotation of Billows 2 and 3 and the differential rotation of the vortex sheet in the horizontal plane at each site result in vortex tube C-D being above Vortex Tube A-B (and Vortex Tube E-F being above Vortex Tube C-D). A last tube with upper end labeled G is seen forming at the lower edge of the Figure 6 thereafter. Their subsequent advection around the Billow 2 and 3 cores entwines these vortices; see the loops at each site, and "figure 8" forms that characterize the vortex structures of any one tube in Figures 6c and 6d. These structures bear a close resemblance to the knots identified in the laboratory by Thorpe (1987, 2002); see the tube interactions yielding two single knots and the paired knots leading to a figure 8 feature in Thorpe (1987, Figure 5, a portion of which is repeated in Figure 11 below).

Figure 7 shows the 3-D evolution of the λ_2 field from above, more negative x, and more positive y of the tube and knot events. As stated above, tube "ends" at Sites C and E are above those at Sites B and D due to the rotations of, and advection by, Billows 2 and 3. The tubes do not "end," however, but are linked to the billow cores leading to their formation. Rotation around Billows 2–4 thereafter leads to multiple, entwined, and roughly orthogonal large-scale vortex alignments (see Movie S2).

KHI evolutions shown in Figures 6 and 7 also reveal the emergence of secondary CI and KHI arising in the outer billow cores and stratified braids between adjacent billows; see Figures 6c–6e within and between adjacent billow cores on both sides of the emerging tubes and knots and the labels and white arrow in Figure 7c. For the chosen parameters, $Ri = 0.05$ and $Re = 5{,}000$, these secondary instabilities of the primary KH billows arise in close proximity and exhibit interactions accompanying their growth to finite amplitudes; see the small-scale scalloped features at left in Figures 6c and 6d that arise from their interactions driven by their

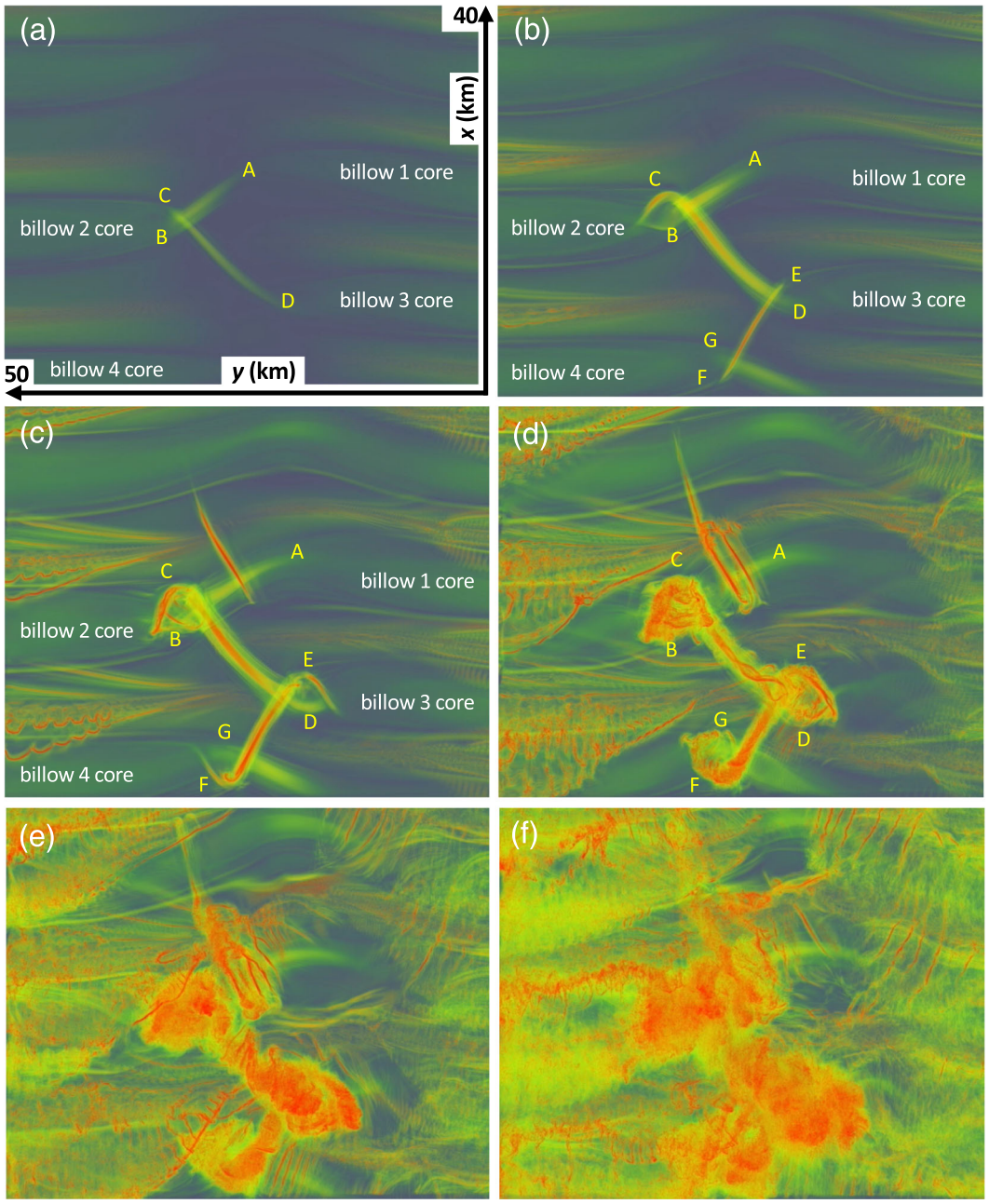

Figure 6. (a–f) KHI tube and knot evolution due to linking of misaligned billows spanning ~2 T_b viewed from above beginning at the initial time in Figures 3 and 4. Shown are volumetric views of λ_2, with small values dark green and large values red in a subset of the full domain. Here, x and y increase toward top and left, respectively, and positive mean ζ_y is toward increasing y (to the left). Panel (a) shows the axes.

initially orthogonal alignments (also see the expanded discussion of Figure 9 in section 4.3 below). Where these secondary instabilities occur in close proximity to the evolving knots (see Figures 7b–7d), they are entrained into the knots and contribute to the complexity and intensity of their dynamics thereafter. We note, in particular, the entrainment of secondary KHI (having initial largely spanwise alignments) into the upper left vortex tube from the lower left in Figures 7b and 7c. We also note the entrainment of initial largely streamwise-aligned CI within the outer KH Billow 4 and 5 cores at right around the right extent of the same underlying vortex tube at right in Figures 7b and 7c. These various vortex dynamics contribute to rapidly evolving and increasingly complex knots that exhibit rapid cascades to smaller scales thereafter.

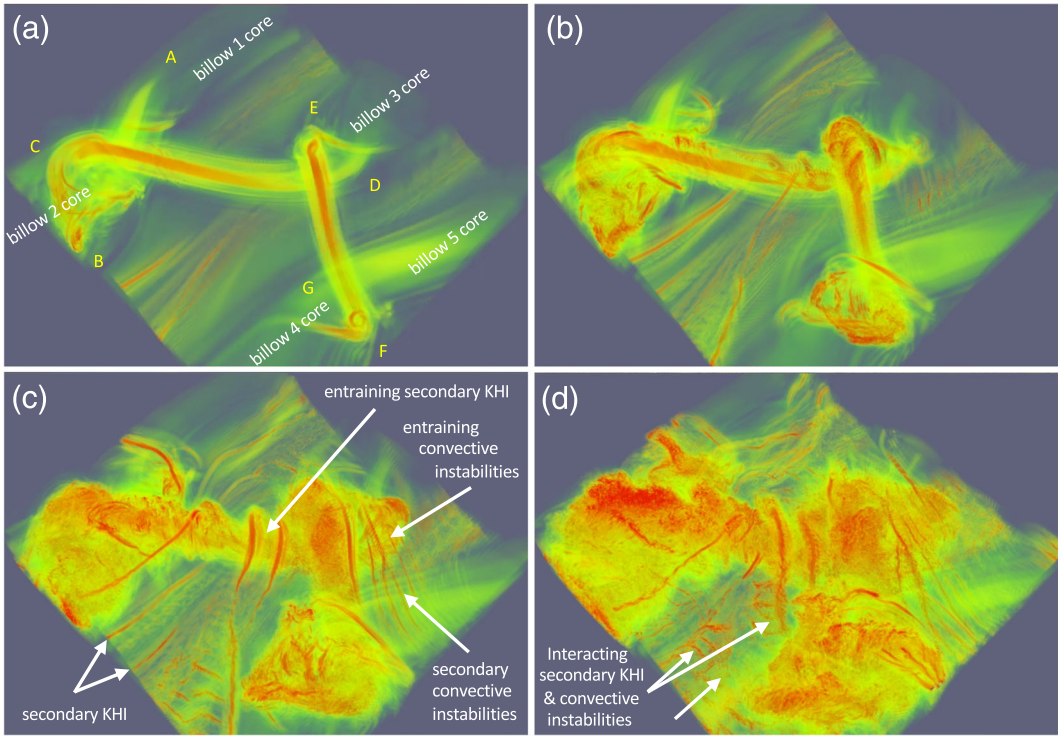

Figure 7. (a–d) Three-dimensional views in a $\Delta x \sim \Delta y \sim$ 25-km subset of the KHI tube and knot evolution from above, behind, and left (more negative x and positive y, relative to Figure 6) spanning ~0.7 T_b beginning at the time shown in Figure 6c. Red denotes large λ_2 and strong vortex rotation. KH billow axes are aligned lower left to upper right and the initial KH billow core vorticity is toward lower left. White arrows show emerging secondary KHI and CI.

It is these dynamics driven by the enhanced vortex dynamics of interacting tubes leading to knots that account for more rapid and more intense turbulence and enhanced enstrophy relative to the secondary instabilities of individual KH billows seen at right in Figure 5.

4.3. Twist Waves: The Path to Turbulence and Dissipation

Entwined, roughly orthogonal vortices exhibit increasingly strong interactions because they are wrapped increasingly tightly as they evolve, and each induces increasing axial (and normal) stretching or compression,

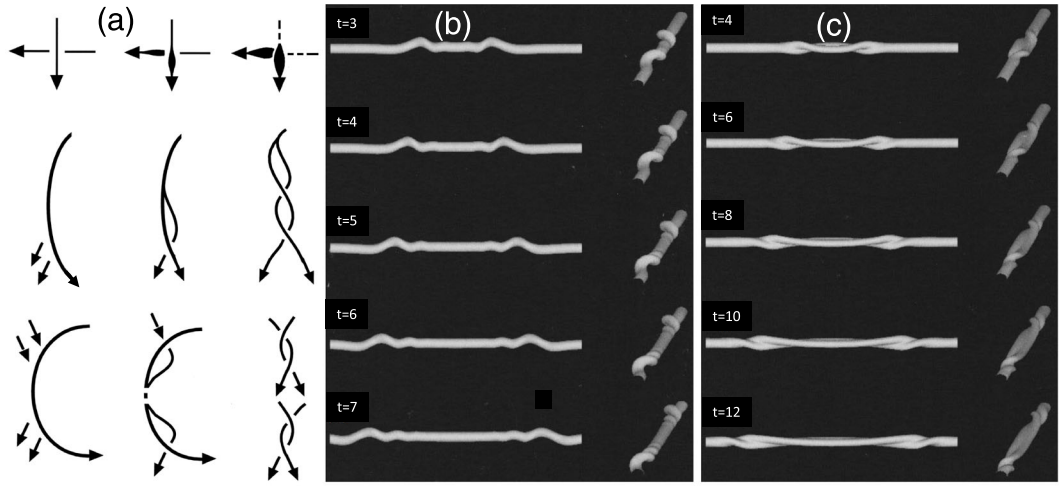

Figure 8. (a) Schematics of vortex interactions by (top) orthogonal vortex stretching and (middle and bottom) perturbations of a vortex tube by one or two vorticity sheets (Fritts et al., 1998). Vortex tube perturbations due to (b) a localized displacement and (c) a localized pinching (Arendt et al., 1997).

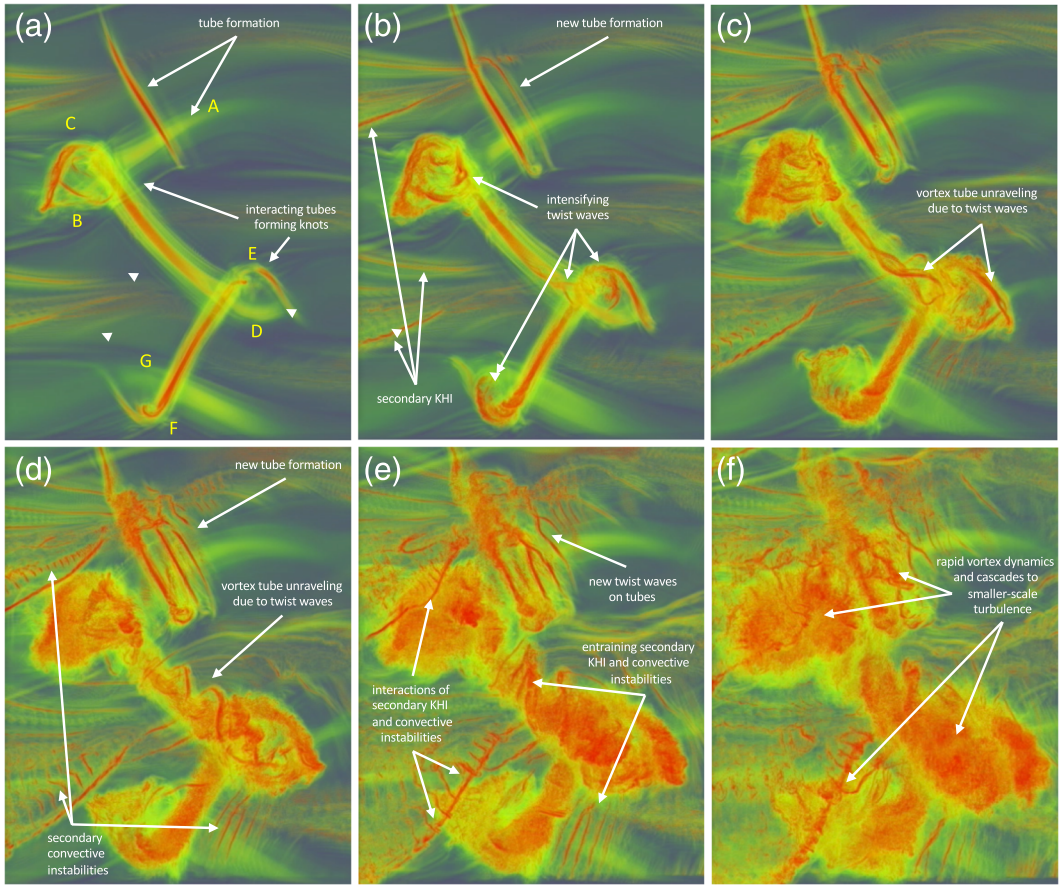

Figure 9. (a–f) Three-dimensional views of a $\Delta x \sim 30$ and $\Delta y \sim 20$-km subset of the λ_2 field from Figures 6c–6e spanning ~1.5 T_b showing the fine structure as KHI tubes, knots, and secondary CI and KHI form and intensify. Specific dynamics are highlighted where they first become apparent. See text for details.

and resulting intensity perturbations, in its neighboring vortices due to differential advection. Seen emerging at early stages of this evolution in Figures 6c and 6d and Figures 7a and 7b are vortex dynamics that exhibit twisting tendencies and spiral or helical structures having opposite rotations at each end of each vortex tube. These perturbations are manifestations of Mode 1 and 2 (and perhaps higher mode) Kelvin vortex waves, or "twist waves" (Kelvin, 1880), and their opposite rotations at each end of each vortex tube indicate inward propagation in each case.

As noted by Arendt et al. (1997) and Fritts et al. (1998), Mode 1 and 2 twist waves are also prevalent in emerging and evolving turbulence fields arising from GW breaking. Importantly, both Modes 1 and 2 appear to play prominent roles in more general vortex dynamics driving turbulence generation at larger scales in sheared and stratified geophysical flows. Key elements include (1) intensification and roll-up of vortex sheets, (2) interactions of adjacent vortices and perturbations of vortex rotational tendencies that can spawn various twist waves, and (3) unraveling and fragmentation of vortices due to twist waves yielding a continuing cascade to smaller-scale vortices. The primary dynamics are shown with subsets of vortex perturbation and interaction schematics from Arendt et al. (1997) and Fritts et al. (1998) in Figure 8 and comprise the major drivers of the cascade of energy and enstrophy to smaller scales in the inertial range of turbulence. The flow of energy and enstrophy to dissipation scales accompanying large-scale KHI begins with the roll-up of a large-scale unstable shear layer defined by mean and local GW shears. Large-scale KH billows arise by accumulating vorticity in the initial shear layer in tight cores that entrain air from above and below. For sufficiently small *Ri* and large *Re*, regions of overturning initiate secondary, counterrotating CI within the outer billow cores and smaller-scale secondary KHI that arise on thin, unstable stratified and sheared braids around and between adjacent large-scale KHI. Where the larger-scale shears are discontinuous,

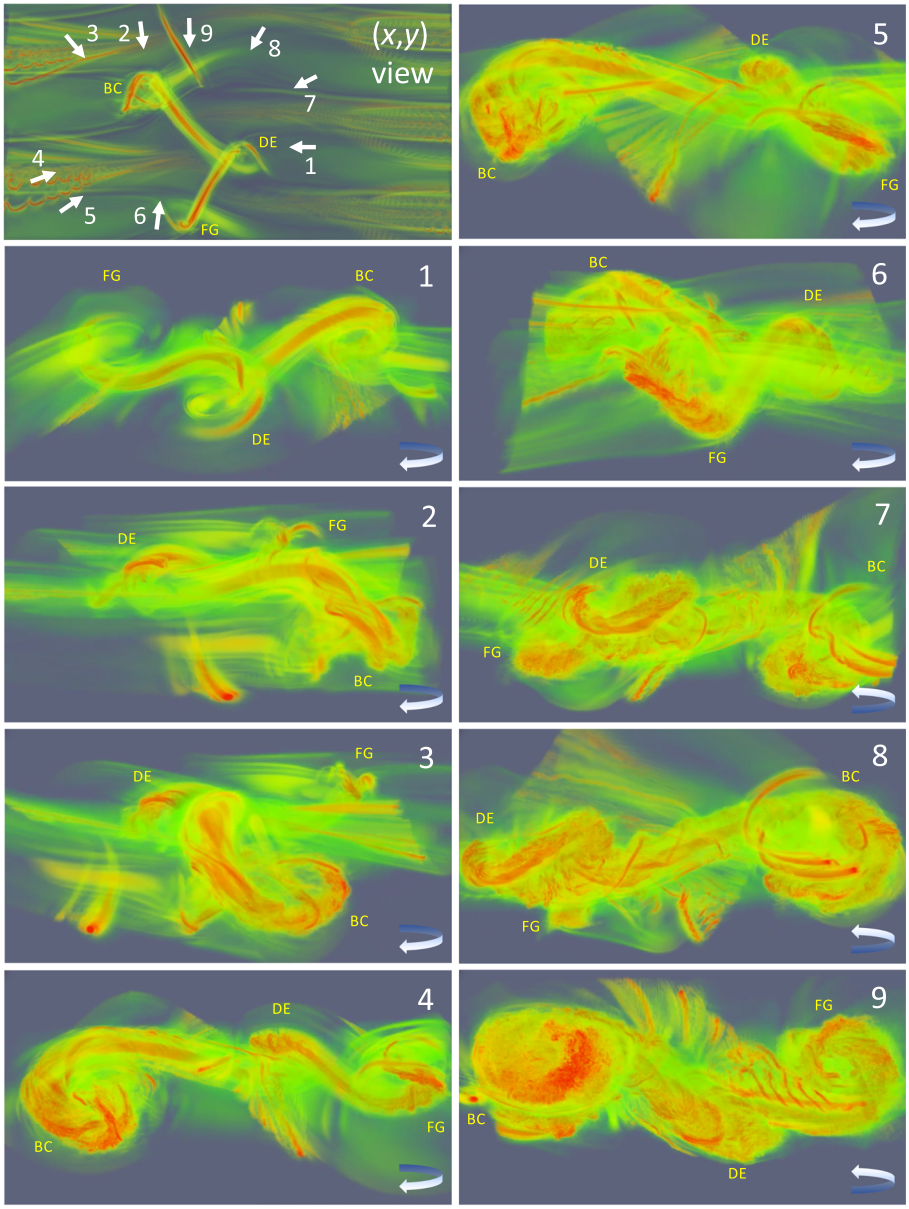

Figure 10. (top left) Viewing of the evolving dynamics shown in Movie S3 at nine times labeled 1–9 shown with increasing z upward, viewed from the side and slightly above and below the (x, y) plane at $z = 0$ in a $\Delta x \sim \Delta y \sim 25$-km volume. Rotation is clockwise viewed from above as in previous figures and is shown with respect to the (x, y) plane at $z = 0$ at lower right in each panel.

misaligned large-scale KH billow growth initiates vortex tubes and knots, due to tilted and deformed vortex sheets, as discussed above. Thereafter, these various vortex structures exhibit a wide range of orientations and scales in close proximity that promote multiple variants of the vortex interactions discussed in relation to Figure 8 that drive the cascade of energy and enstrophy to smaller scales.

The hierarchy of emerging vortices and their subsequent interactions and consequences as they intensify in close proximity (some of which were discussed above) are highlighted in zoomed views of the evolving tubes and knots seen at bottom center in Figures 6c–6f and shown in Figure 9. Specific components include the following (also see Movies S1–S3):

1. roughly orthogonal vortex tubes arising on twisted vortex sheets between misaligned KH billows that extend to adjacent billows along the 2-D billow motions in time (Figure 9a),

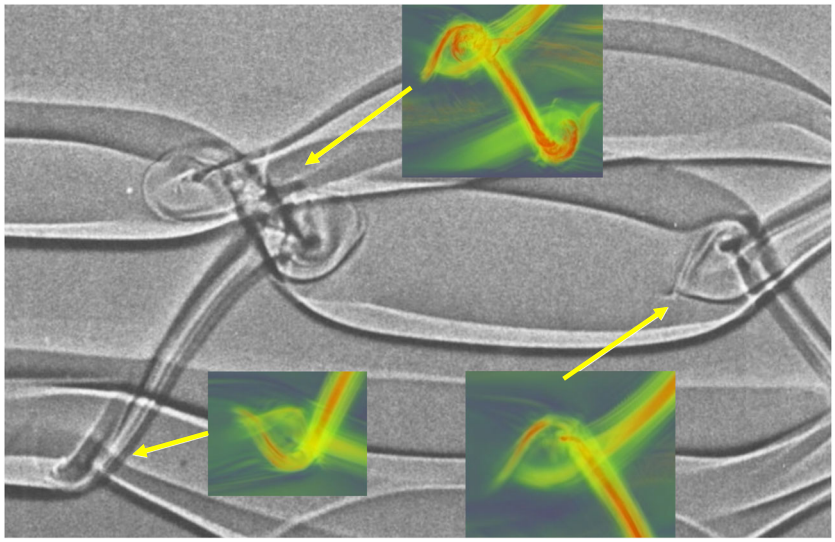

Figure 11. Thorpe (1987) shadowgraph image of KHI interactions leading to tubes and knots (see yellow arrows). Colored insets show modeled features discussed in the text that closely resemble the observed features.

2. linking of vortex tube "ends" where rotation by the common KH billow core and mutual advection and stretching/compression along the axis of each tube by the other initiate large-amplitude Mode 2 twist waves leading to vortex tube fragmentation (Figures 9b and 9c),
3. emergence of secondary CI and KHI, normal to and along the billow axes in each KH billow core at larger and smaller x away from the tube and knot dynamics (Figures 9b–9d),
4. entrainment around, and stretching and intensification of, secondary CI and KHI around the larger-scale tubes and knots (Figure 9e), and
5. interacting adjacent larger- and smaller-scale vortices leading to new twist waves at ever smaller scales that account for the flux of energy through the inertial range (Figure 9f).

Another perspective on this KHI evolution is provided in Figure 10 showing 3-D imaging viewed more nearly in the plane of the KHI dynamics spanning the same interval as shown in Movie S3 and from above in Figures 6, 7, and 9. This enables a better appreciation of the KH billow, tube, and knot depths and their excursions and tilts with respect to the (x, y) plane. These images rotate around the z axis clockwise with respect to the KHI event in the top left panel with increasing z upward to be consistent with the images described above. The top left panel shows that the first six images occur within the first full rotation seen from above the (x, y) plane ($z < 0$), with two subsets, Images 1–3 and Images 4–6, showing partial rotations with common features. A third image subset at the beginning of the second rotation of the FOV includes Images 7–9 seen from below ($z < 0$). Knots are labeled by the two tube ends leading to their formation.

The first subset shows vortex knot DE moving from center to left back and vortex knot BC moving from right back to center. These images show a vortex tube having the same vorticity along its axis (toward knot BC), but exhibiting Mode 2 twist waves at each end having opposite helicity, hence inward propagation in each case (see Figure 8c). The second subset shows similar behavior, with tube vorticity toward knot FG and also having converging Mode 2 twist waves at each end. The tubes and twist wave dynamics share common features because the KH billow rotation is common to both tubes. Both image subsets (especially Images 3–6) also show secondary KHI emerging along the vorticity sheet trailing and extending up and over the KH billow accounting for knot BC rotation. Their alignments are along the KH billow away from the knot, but are entrained up and over Tube A-B within the knot vorticity field.

Images 7–9 show a more advanced stage of the knot evolution revealing the vortex evolution along Tube A-B and of knot BC. Tube A-B in Images 7 and 8 now exhibits strong twist waves on the tube and secondary KHI entrained from the opposite side (cf. to the view in Image 5). Knot BC likewise exhibits vortex fragmentation and generation of smaller-scale vortices in Images 7 and 8, and Images 8 and 9 show emerging interactions among the secondary CI and KHI in the outer billow leading knot FG.

The depths of these dynamics are comparable to or exceed those of KH billows not undergoing interactions leading to tube and knot dynamics because they extend around the outer edges of the interacting KH billows, which have depths of ~0.5 λ_h or larger for Ri ~ 0.05 and sufficiently high Re in the absence of tube and knot dynamics (Thorpe, 1973a).

5. Relation to Previous Studies and Significance

Studies of KHI in oceans, lakes, the atmosphere, and the laboratory have a long history. Atmospheric observations of KHI revealed in thin cloud layers in the troposphere and mesosphere relevant to the modeling described above spanned ~70 years. Key observations included recognition of the underlying KHI dynamics arising from unstable shear flows and the tendency for background variability in the shear layer to contribute to KHI responses having limited extents along their axes (Ludlam, 1967; Scorer, 1951; Witt, 1962). However, those studies were not able to reveal the smaller scale dynamics arising from KHI interactions at sites where billow cores were misaligned. Subsequent tilt-tank shear flow studies reported by Thorpe (1985, 1987) provided the first clues to these dynamics. These experiments revealed small-scale features that Thorpe called tubes and knots where KH billow cores were misaligned or exhibited pairing in localized regions along their axes. Thorpe (2002) recognized the relationship between misaligned billow clouds and the laboratory examples of billow interactions leading to more rapid, and potentially enhanced, turbulence transitions and suggested that such dynamics must be widespread in the atmosphere.

Misaligned KH billow cores were observed in earlier imaging of KHI seen in the OH airglow layer at a typical altitude of ~87 km, but the imaging resolution in those cases was not sufficient to reveal these smaller-scale dynamics (Hecht et al., 2005, 2014). Modulated KH billows were also observed at much higher resolution in the polar mesospheric cloud (PMC) layer over Scandinavia (Baumgarten & Fritts, 2014), but these had λ_h ~ 3–5 km, a relatively large Ri ~ 0.2, slow and weak turbulence transitions, and no evidence of strong interactions among adjacent billows.

The first high-resolution atmospheric observation of misaligned and interacting KH billows leading to a tube and knot event was the serendipitous imaging of large-scale KH billows (λ_h ~ 10 km) over ALO on 1 March 2016 described in detail by H20 and summarized above. H20 employed difference imaging that was able to resolve initial billow interactions at larger scales and the emergence of additional smaller-scale vortex features as the billows evolved. Specifically, the ALO imaging captured vortex tubes prior to and accompanying linking of adjacent billows (see the yellow lines in Figure 1 images at 32:55 and thereafter). They also revealed apparent twisting by rotating KH billow cores leading to interacting and intertwining of initial vortex tubes (see the green loops at 34:47 and 36:19 in Figure 1), based on the earlier modeling images in Figure 6. Additionally, ALO imaging resolved initial SCI within the KH billow cores as the billows attained finite amplitudes (see the blue lines at later times in Figure 1). Successive images revealed additional small-scale structures suggesting additional vorticity dynamics and turbulence thereafter, but 4 × 4 pixel binning, ~7.4-s exposures, and ~55-m/s advection caused smearing over ~400 m especially along the mean advection. Nevertheless, the early stages of this event confirm the expectations for such dynamics and their likely influences throughout the atmosphere wherever KHI arises and attains sufficiently small Ri and large Re.

Comparisons of the modeled KHI tube and knot features with those observed by Thorpe (1987) also reveal striking agreement in several respects. A subsection of Figure 5 from Thorpe (1987) revealing four knots having varying character is shown in Figure 11. Also shown are overlaid images of three modeled tubes and emerging knots in the (x, y) plane from Figures 6b and 6c that most closely resemble those seen in the laboratory at the time shown. These reveal quite remarkable agreement in several key features.

Those seen in the knots at bottom left and middle right include (1) evidence of twisting of the initial tube "ends" by the associated KH billow in both cases; (2) variations in tube intensities along their axes indicating differential advection and axial compression and stretching on either side by the orthogonal tube, as shown at top in Figure 8a; and (3) indications of initial smaller-scale vorticity structures and twist waves in both knots that arise where the tube cores are perturbed by stretching and compression along their axes due to the adjacent tube.

Comparing the laboratory and modeled "figure 8" structures at top in Figure 11, we again note a number of features that appear to agree well. These include (1) striations along the tube axes entering the lower knot in the figure 8 from lower left and similar responses entering the two separate laboratory knots from the right and/or left and (2) clear twist waves in both knots in the figure 8 along the tube internal to the knot at top in the laboratory image and the modeled response (see the upper edge of the red tube) and both within the knot and along both tubes in the laboratory image and the modeled response at bottom.

While these comparisons are necessarily qualitative, given the different laboratory and modeled environments and the different imaging, the qualitative agreement is surprising and significant. The results suggest that KH billow interactions where billow cores are misaligned have similar implications wherever they are sufficiently strong accompanying small *Ri* and large *Re*. Evidence in the modeling for much more rapid and intense vorticity dynamics accompanying tube and knot evolutions than accompanies secondary instabilities of individual KH billows, and the expectation that such dynamics are likely common, given the small coherence lengths of KH billows in the atmosphere of ~3–8 λ_h, also imply that turbulence arising due to KH tube and knot dynamics may be a statistically significant contributor to the total contributions by KHI throughout the atmosphere, and perhaps where KHI exhibits spatial modulation in other fluids. However, further quantification of these assessments requires direct numerical simulations (DNS) of these dynamics that can directly assess the energy dissipation rates accompanying these dynamics and evaluate dependence on, and their statistics as functions of, the relevant nondimensional parameters. These DNS modeling efforts are now complete and will be reported elsewhere.

6. Summary and Conclusions

KH instabilities have been known for many years to play significant roles in atmospheric dynamics extending from Earth's surface into the lower thermosphere. Early observations also suggested limited extents of KH billows along their axes, but with unknown causes and consequences. Laboratory studies by Thorpe (1985, 1987) and Caulfield et al. (1996) revealed that regions where KH billows are initially misaligned enable interactions than can proceed more quickly, and with greater intensities, than the secondary instabilities of individual KH billows. These dynamics comprise what Thorpe (1985) called tubes and knots, were first identified in high-resolution OH imaging at ~88 km in the mesosphere in March 2016 and described by H20, and were the motivations for the modeling described here.

Our modeling confirmed that KH tubes and knots involve dynamics that proceed more rapidly, and are more intense, than secondary instabilities accompanying individual KH billows. They also enabled detailed assessments of the evolving dynamics at larger and smaller scales, the character of the evolving vorticity fields, and the interactions driving their forms and evolutions. Specific comparisons of modeled tube and knot features with apparent features seen in the earlier laboratory studies revealed close agreement and appear to confirm the dynamical pathways from laminar to turbulent flows accompanying these dynamics. Additional modeling studies employing DNS are expected to further quantify the importance of these dynamics, their turbulence intensities and statistics, and their various roles in atmospheric transport, structure, and variability, and expected responses in other geophysical fluids.

Data Availability Statement

High-resolution figures and the three volumetric animations of these KHI dynamics, Movies S1–S3, are available as supporting information. ALO imaging and model data required to reproduce the results presented here are available at Zenodo (https://doi.org/10.5281/zenodo.4023307).

Acknowledgments

Research described here was supported by AFOSR, National Science Foundation, and NASA grants cited in GEMS. Computational resources were provided by the DoD High Performance Computing Modernization Program in association with AFOSR support. We thank three anonymous reviewers for comments that helped us improve the presentation of results.

References

Andreassen, Ø., Hvidsten, P. Ø., Fritts, D. C., & Arendt, S. (1998). Vorticity dynamics in a breaking gravity wave. Part 1. Initial instability evolution. *Journal of Fluid Mechanics*, *367*, 27–46.

Arendt, S., Fritts, D. C., & Andreassen, Ø. (1997). The initial value problem for Kelvin twist waves. *Journal of Fluid Mechanics*, *344*, 181–212.

Baumgarten, G., & Fritts, D. C. (2014). Quantifying Kelvin-Helmholtz instability dynamics observed in noctilucent clouds: 1. Methods and observations. *Journal of Geophysical Research: Atmospheres*, *119*, 9324–9337. https://doi.org/10.1002/2014JD021832

Browning, K. A., & Watkins, C. D. (1970). Observations of clear air turbulence by high power radar. *Nature*, *227*(5255), 260–263. https://doi.org/10.1038/227260a0

Caulfield, C. P., Yoshida, S., & Peltier, W. R. (1996). Secondary instability and three-dimensionalization in a laboratory accelerating shear layer with varying density differences. *Dynamics of Atmospheres and Oceans*, *23*, 139–153.

Corcos, G. M., & Sherman, F. S. (1976). Vorticity concentration and the dynamics of unstable free shear layers. *Journal of Fluid Mechanics*, *73*, 241–246.

Dong, W., Fritts, D. C., Lund, T. S., Wieland, S. A., & Zhang, S. (2020). Self-acceleration and instability of gravity wave packets: 2. two-dimensional packet propagation, instability dynamics, and transient flow responses. *Journal of Geophysical Research: Atmospheres*, *125*, e2019JD030691. https://doi.org/10.1029/2019JD030691

Drazin, P. G. (1958). The stability of a shear layer in an unbounded heterogeneous inviscid fluid. *Journal of Fluid Mechanics*, *4*, 214–224.

Dunkerton, T. J. (1997). Shear instability of internal inertia-gravity waves. *Journal of the Atmospheric Sciences*, *54*, 1628–1641.

Felten, F. N., & Lund, T. S. (2006). Kinetic energy conservation issues associated with the collocated mesh scheme for incompressible flow. *Journal of Computational Physics*, *215*, 465–484. https://doi.org/10.1016/j.jcp.2005.11.009

Fritts, D. C., & Alexander, M. J. (2003). Gravity wave dynamics and effects in the middle atmosphere. *Reviews of Geophysics*, *41*(1), 1003. https://doi.org/10.1029/2001RG000106

Fritts, D. C., Arendt, S., & Andreassen, O. (1998). Vorticity dynamics in a breaking internal gravity wave, 2. Vortex interactions and transition to turbulence. *Journal of Fluid Mechanics*, *367*, 47–65.

Fritts, D. C., Baumgarten, G., Wan, K., Werne, J. A., & Lund, T. (2014). Quantifying Kelvin-Helmholtz instability dynamics observed in noctilucent clouds: 2. Modeling and interpretation of observations. *Journal of Geophysical Research: Atmospheres*, *119*, 9324–9337. https://doi.org/10.1002/2014JD021833

Fritts, D. C., & Rastogi, P. K. (1985). Convective and dynamical instabilities due to gravity wave motions in the lower and middle atmosphere: Theory and observations. *Radio Science*, *20*, 1247–1277. https://doi.org/10.1029/RS020i006p01247

Fritts, D. C., Wan, K., Franke, P., & Lund, T. (2012). Computation of clear-air radar backscatter from numerical simulations of turbulence: 3. Off-zenith measurements and biases throughout the lifecycle of a Kelvin-Helmholtz instability. *Journal of Geophysical Research*, *117*, D17101. https://doi.org/10.1029/2011JD017179

Fritts, D. C., Wan, K., Werne, J., Lund, T., & Hecht, J. H. (2014). Modeling the implications of Kelvin-Helmholtz instability dynamics for airglow observations. *Journal of Geophysical Research: Atmospheres*, *119*, 8858–8871. https://doi.org/10.1002/2014JD021737

Fritts, D. C., Wang, L., Werne, J., Lund, T., & Wan, K. (2009). Gravity wave instability dynamics at high Reynolds numbers, 2: Turbulence evolution, structure, and anisotropy. *Journal of the Atmospheric Sciences*, *66*, 1149–1171. https://doi.org/10.1175/2008JAS2727.1

Fritts, D. C., Wang, L., & Werne, J. A. (2013). Gravity wave-fine structure interactions. Part I: Influences of fine structure form and orientation on flow evolution and instability. *Journal of the Atmospheric Sciences*, *70*, 3710–3734. https://doi.org/10.1175/JAS-D-13-055.1

Germano, M., Piomelli, U., Moin, P., & Cabot, W. H. (1991). A dynamic subgrid-scale eddy viscosity model. *Physics of Fluids A: Fluid Dynamics*, *3*, 1760–1765.

Gossard, E. E., Richter, J. H., & Jensen, D. R. (1973). Effect of wind shear on atmospheric wave instabilities revealed by FM/CW radar observations. *Boundary-Layer Meteorology*, *4*, 113–131.

Hecht, J. H., Fritts, D. C., Gelinas, L. J., Rudy, R. J., Walterscheid, R. L., & Liu, A. Z. (2020). Kelvin-Helmholtz billow interactions and instabilities in the mesosphere over the Andes Lidar Observatory: 1. Observations. *Journal of Geophysical Research: Atmospheres*, *125*, e2020JD033414. https://doi.org/10.1029/2020JD033414

Hecht, J. H., Fritts, D. C., Gelinas, L. J., Rudy, R. J., Walterscheid, R. L., Liu, A. Z., & Thorpe, S. A. (2020). Kelvin-Helmholtz billow interactions and instabilities in the mesosphere over the Andes Lidar Observatory: 1. Observations. *Journal of Geophysical Research: Atmospheres*, *119*, 9359–9375. https://doi.org/10.1002/2014JD021833

Hecht, J. H., Fritts, D. C., Wang, L., Gelinas, L. J., Rudy, R. J., Walterscheid, R. L., & Franke, S. J. (2018). Observations of the breakdown of mountain waves over the Andes Lidar Observatory at Cerro Pachon on 8/9 July 2012. *Journal of Geophysical Research: Atmospheres*, *123*, 276–299. https://doi.org/10.1002/2017JD027303

Hecht, J. H., Liu, A. Z., Walterscheid, R. L., & Rudy, R. J. (2005). Maui mesosphere and lower thermosphere (Maui MALT) observations of the evolution of Kelvin-Helmholtz billows formed near 86 km altitude. *Journal of Geophysical Research*, *110*, D09S10. https://doi.org/10.1029/2003JD003908

Hecht, J. H., Wan, K., Gelinas, L. J., Fritts, D. C., Walterscheid, R. L., Franke, S. J., et al. (2014). The lifecycle of instability features measured from the Andes Lidar Observatory over Cerro Pachon on March 24, 2012. *Journal of Geophysical Research: Atmospheres*, *119*, 8872–8898. https://doi.org/10.1002/2014JD021726

Helmholtz, H. (1868). On discontinuous movements of fluids, translated from German by F. Guthrie. *Philosophical Magazine*, *36*, 337–346.

Holmboe, J. (1962). On the behaviour of symmetric waves in stratified shear layers. *Geophysical Publication*, *24*, 67–113.

Holt, J. T. (1998). Experiments on Kelvin-Helmholtz billows influenced by boundaries. *Geophysical and Astrophysical Fluid Dynamics*, *89*, 205–233.

Jeong, J., & Hussain, F. (1995). On the identification of a vortex. *Journal of Fluid Mechanics*, *285*, 69–94.

Kelvin, L. (1880). Vibrations of a columnar vortex. *Philosophical Magazine*, *10*, 155–168.

Kelvin, W. (1871). The influence of wind on waves in water supposed frictionless. *Philosophical Magazine*, *42*, 368–374.

Klaassen, G. P., & Peltier, W. R. (1985). The onset of turbulence in finite-amplitude Kelvin-Helmholtz billows. *Journal of Fluid Mechanics*, *155*, 1–35.

Lehmacher, G. A., Guo, L., Kudeki, E., Reyes, P. M., Akgiray, A., & Chau, J. L. (2007). High-resolution observations of mesospheric layers with the Jicamarca VHF radar. *Advances in Space Research*, *40*(6), 734–743. https://doi.org/10.1016/j.asr.2007.05.059

Lelong, M.-P., & Dunkerton, T. J. (1998). Inertia-gravity wave breaking in three dimensions. Part I: Convectively stable waves. *Journal of the Atmospheric Sciences*, *55*, 2473–2488.

Ludlam, F. H. (1967). Billow clouds and their relation to clear air turbulence. *Quarterly Journal of the Royal Meteorological Society*, *93*, 419–435.

Moin, P., Squires, K. D., Cabot, W. H., & Lee, S. (1991). A dynamic subgrid-scale model for compressible turbulence and scalar transport. *Physics of Fluids A*, *3*(11), 2746–2757. https://doi.org/10.1063/1.858164

Palmer, T. L., Fritts, D. C., & Andreassen, O. (1996). Evolution and breakdown of Kelvin-Helmholtz billows in stratified compressible flows, II: Instability structure, evolution, and energetics. *Journal of the Atmospheric Sciences*, *53*, 3192–3212.

Patnaik, P. C., Sherman, F. S., & Corcos, G. M. (1976). A numerical simulation of Kelvin-Helmholtz waves of finite amplitude. *Journal of Fluid Mechanics*, *73*, 215–240.

Pfrommer, T., Hickson, P., & She, C.-Y. (2009). A large-aperture sodium fluorescence lidar with very high resolution for mesopause dynamics and adaptive optics studies. *Geophysical Research Letters*, *35*, L15831. https://doi.org/10.1029/2009GL038802
Richter, J. H. (1969). High-resolution tropospheric radar sounding. *Radio Science*, *4*, 1261–1268.
Schowalter, D. G., Van Atta, C. W., & Lasheras, J. C. (1994). A study of streamwise vortex structure in a stratified shear flow. *Journal of Fluid Mechanics*, *281*, 247–291.
Scorer, R. (1951). Billow clouds. *Quarterly Journal of the Royal Meteorological Society*, *77*, 235–240.
Scorer, R., & Wexler, H. (1963). *A colour guide to clouds*. Oxford: Pergamon Press.
Scorer, R. S. (1969). Billow mechanics. *Radio Science*, *4*, 1299–1307.
Thorpe, S. A. (1971). Experiments on the instability of stratified shear flows: Miscible fluids. *Journal of Fluid Mechanics*, *46*, 299–320.
Thorpe, S. A. (1973a). Turbulence in stably stratified fluids: A review of laboratory experiments. *Boundary-Layer Meteorology*, *5*(95–119), 541–549.
Thorpe, S. A. (1973b). Experiments on instability and turbulence in a stratified shear flow. *Journal of Fluid Mechanics*, *61*, 731–751.
Thorpe, S. A. (1978). The near-surface ocean mixing layer in stable heating conditions. *Journal of Geophysical Research*, *83*, 2875–2885.
Thorpe, S. A. (1985). Laboratory observations of secondary structures in Kelvin-Helmholtz billows and consequences for ocean mixing. *Geophysical and Astrophysical Fluid Dynamics*, *34*, 175–199.
Thorpe, S. A. (1987). Transitional phenomena and the development of turbulence in stratified fluids: A review. *Journal of Geophysical Research*, *92*, 5231–5248.
Thorpe, S. A. (2002). The axial coherence of Kelvin-Helmholtz billows. *Quarterly Journal of the Royal Meteorological Society*, *128*, 1529–1542.
Thorpe, S. A. (2005). *The Turbulent Ocean* (p. 439). Cambridge: Cambridge University Press.
Thorpe, S. A., Hall, A. J., Taylor, C., & Allen, J. (1977). Billows in Loch Ness. *Deep Sea Research*, *24*, 371–379.
Werne, J., & Fritts, D. C. (1999). Stratified shear turbulence: Evolution and statistics. *Geophysical Research Letters*, *26*, 439–442. https://doi.org/10.1029/1999GL900022
White, F. M. (1974). *Viscous fluid flow*. New York: McGraw-Hill.
Witt, G. (1962). Height, structure and displacements of noctilucent clouds. *Tellus*, *14*, 1–18.
Woods, J. D. (1968). Wave-induced shear instability in the summer thermocline. *Journal of Fluid Mechanics*, *32*, 791–800.
Woods, J. D. (1969). On Richardson's number as a criterion for laminar-turbulent-laminar transition in the ocean and atmosphere. *Radio Science*, *4*, 1289–1298.
Woods, J. D., & Wiley, R. L. (1972). Billow turbulence and ocean microstructure. *Deep Sea Research*, *19*, 87–121.